





# Self-Healing Predictive Control of Battery System in Naval Power System With Pulsed Power Loads

Mohsen Hosseinzadehtaher , *Student Member, IEEE*, Ahmad Khan , *Student Member, IEEE*, Mitchell Easley, *Student Member, IEEE*, Mohammad B. Shadmand , *Senior Member, IEEE*, and Poria Fajri , *Member, IEEE*

**Abstract**—This article presents a model predictive self-healing control (MPSC) scheme for battery system interfaced dual active bridge (DAB) converter in navy ship power system (NSPS) with pulsed power loads (PPLs). The voltage and frequency of NSPS are vulnerable to PPLs energization. A properly controlled battery system with fast dynamic response can mitigate this vulnerability. Model predictive control (MPC) is a potential solution for the battery system interfaced DAB converter to achieve fast dynamic response and mitigate disturbances imposed to the NSPS by PPLs. However, conventional MPC framework suffers from current prediction error due to the pulsating AC-link inductor's voltage profile in DAB converter. This article proposes a self-healing control loop that utilizes the feasible range of power transfer in conjunction with the AC-link inductor's voltage profile. The proposed method can validate and autonomously correct the predicted current and phase shift in DAB converter interfaced a battery system. The proposed control scheme on DAB converter prevents voltage and frequency collapse in a hybrid AC/DC NSPS particularly during the PPL energization. The system stability is studied based on Lyapunov stability analysis. The theoretical concepts are validated by several case studies implemented on a hardware-in-the-loop (HIL) testbed of a NSPS. The case studies demonstrate voltage and frequency regulation of the NSPS with fast dynamic response during PPLs energization. The proposed MPSC performance is compared with proportional-integral (PI) based control for DAB in NSPS with PPLs.

**Index Terms**—Navy ship power system, pulsed power loads, MPC, dual active bridge converter.

## I. INTRODUCTION

NAVY Ship Power System (NSPS) commonly consists of loads with different behaviors. These loads can be categorized such as ship propulsion system, pulsed power loads (PPLs),

Manuscript received March 26, 2020; revised June 25, 2020; accepted July 25, 2020. Date of publication August 5, 2020; date of current version May 21, 2021. This publication was made possible by grant # NPRP 12S-0226-190158 (model predictive self-healing control section) from Qatar National Research Fund (a member of the Qatar Foundation). The statement made herein are solely the responsibility of the authors. (*Corresponding author: Mohammad B. Shadmand.*)

Mohsen Hosseinzadehtaher, Ahmad Khan, and Mohammad B. Shadmand are with the Department of Electrical and Computer Engineering, University of Illinois at Chicago, Chicago, IL 60637 USA (e-mail: mhosse5@uic.edu; ahmad20@uic.edu; shadmand@uic.edu).

Mitchell Easley is with the Department of Electrical and Computer Engineering, Kansas State University, Manhattan, KS 66506 USA (e-mail: mitch01@ksu.edu).

Poria Fajri is with the Department of Electrical and Biomedical Engineering, University of Nevada, Reno, NV 89512 USA (e-mail: pfajri@unr.edu).

Color versions of one or more of the figures in this article are available online at <https://ieeexplore.ieee.org>.

Digital Object Identifier 10.1109/TEC.2020.3014294

etc. Some of NSPS' loads do not have significant fluctuating patterns, which are considered steady-state loads. However, others require large amount of energy in a very short duration that are known as PPLs. The common PPLs in NSPS are: electromagnetic guns, electromagnetic aircraft launch systems, free electron lasers, radar, and sonar [1]. Thus, due to existence of PPLs, the transient stability of NSPS should be considered when designing the control schemes of NSPS [2]–[4]. Due to the inherent slow dynamic response of synchronous generator in NSPS, considerable voltage and frequency deviations occur due to PPLs energization. If not properly addressed, this undesired voltage and frequency deviations can cause collapse of the voltage sensitive loads or even the whole NSPS.

Energy storage systems (ESS) such as battery banks and super-capacitors are typically used in NSPS for mitigating the voltage and frequency fluctuations due to PPLs [5]–[7]. Dual active bridge (DAB) converter is known as a proper power electronics interface for ESS in response to fast transient loads such as PPLs [8]. Due to periodic sudden changes of PPLs which requires frequent charging and discharging of ESSs, a high efficiency power conversion unit, such as DAB converter, is recommended [9]. Although the DAB converter features can be leveraged for ESS to realize fast restoration of voltage and frequency in NSPS, but the drawback of this converter is its control complexity [10].

Several control schemes have been proposed in literature for DAB converter. A voltage control with power balancing mechanism is proposed in [11] for solid state transformer (SST) based on parallel DAB modules. The proposed PI based control scheme regulates DC-Bus voltage and determines the proper phase shift. In [12], power transfer in resonant DAB converter is enabled by regulating the phase shift and resonant tank currents in this system. In order to make the control process easier, the authors have used a *dq* framework to convert all ac state variables to dc states with slow dynamics. Hence, for controlling phase shift and tank currents, three PI controllers are used. It is worth mentioning that the DAB converter highly nonlinear plant for a PI controller results in slow dynamic response which may fail in response to fast transient loads such as PPLs [13]. The transient response of a single-side modulation and symmetric double-side modulation of a DAB converter are studied in [14]; a modified asymmetric double-side modulation is then proposed for improving the dynamic response. In [15], a curved switching surface has been presented for control of DAB converter for

TABLE I  
EXISTING DAB CONVERTER CONTROL APPROACHES

Control Objective	Features	Drawbacks
Voltage and Power Balance Control for a Converter-Based Solid-State Transformer [11].	<ul style="list-style-type: none"> <li>Regulating the DC-Bus voltage and determining the proper phase shift.</li> <li>Balancing the rectifier capacitor voltages and the real power through parallel DAB modules.</li> </ul>	<ul style="list-style-type: none"> <li>Slow dynamic response</li> <li>Vulnerable to fail in response to fast transient loads</li> <li>large changing in the operation point cause malfunction for the control scheme</li> </ul>
Modeling and Control of a Resonant Dual Active Bridge with a Tuned CLLC Network [12].	<ul style="list-style-type: none"> <li>Regulating the phase shift and resonant tank currents in this system for transferring the power.</li> <li>Fast simulation</li> <li>Using dq framework to convert all AC state variables to DC states</li> <li>Improving the soft switching range of the converter.</li> </ul>	<ul style="list-style-type: none"> <li>All challenges related to PI-controller tuning</li> <li>Changing the operation point will make problem for tuning</li> </ul>
Optimized Phase-Shift Modulation for Fast Transient Response in a Dual-Active-Bridge Converter [14].	<ul style="list-style-type: none"> <li>Proposing a modified asymmetric double-side modulation for the aim of improving the dynamic response.</li> <li>Minimizing the settling time of the inductor current</li> </ul>	<ul style="list-style-type: none"> <li>Converter gain should be available</li> <li>It has not been tested for close loop system with large load variation</li> </ul>
Fast Transient Boundary Control of the Dual Active Bridge Converter Using the Natural Switching Surface [15].	<ul style="list-style-type: none"> <li>Improving dynamic response to sudden load changes</li> <li>Curved switching surface has been presented for control of DAB converter</li> <li>Fixed-frequency operation</li> <li>Optimizing the design of the high-frequency transformer</li> </ul>	<ul style="list-style-type: none"> <li>The step change is small (less than 4 amperes)</li> <li>Fast transient response is for startup not for large loads</li> <li>No guarantee to work with large load pulsation</li> </ul>
Enhanced Load Step Response for a Bidirectional DC-DC Converter [16].	<ul style="list-style-type: none"> <li>Minimizing the DC-Bus capacitance</li> <li>Utilizing harmonic modeling strategy</li> </ul>	<ul style="list-style-type: none"> <li>linearized model will have challenges facing with large disturbance</li> <li>Tuning effort of PI-based controller can be challenging</li> <li>The controller gain will not be remained valid for different operation points.</li> </ul>

improving dynamic response to sudden load changes. Furthermore, the authors of [16], have provided a method for enhancing the transient response of DAB converters to sudden load disturbances by utilizing harmonic modeling strategy. However, the downside of these PI-based control methods are tuning effort and the assumptions that the controller gain will remain valid for different operation points as the equilibrium point changes. These available controllers along with their features and drawbacks are summarized in Table. I.

Model Predictive control (MPC) is one of the attractive control approaches in power electronics applications that has been widely used in industry and academia [17]. This is due to MPC fast dynamical response and ability in solving multi-objective constraints optimization problems with substantially less effort in gain tuning or re-tuning process compared to linear controllers [18]–[22]. Moreover, for the DAB converter, very few MPC frameworks have been reported in the literature due to challenges associated with design of MPC for DAB converter. In fact, unlike MPC of other power electronics application, conventional MPC framework is not applicable for DAB converter and requires modification in the algorithm. For instance, [23] introduces a predictive control approach that eliminates transient dc offset currents that have been superimposed on the high frequency transformer currents in one switching cycle. This protects the high frequency transformer from reaching saturation. However, this approach is based on increasing the control bandwidth which is a challenging requirement for application of MPC on DAB converter for PPLs. Authors in [24] have introduced a moving discretized-control-set MPC approach for DAB converters. The purpose of this control approach is to regulate load voltage of the DC microgrid and minimize the DAB

converter high frequency transformer peak current. However, the MPC model is based on simplified DAB averaged model that is subjected to inaccuracies given DAB converter's high nonlinearity. Therefore, up to the best knowledge of the authors, the limited existing MPC frameworks are not best fit for the DAB converter in applications such as PPLs and this is due to DAB topology and its non-linear behavior specially when an accurate prediction of AC link inductor current is required. Thus, the main contribution of this paper is to address the challenges associated with design of MPC framework for DAB in NSPS in response to voltage and frequency deviations due to PPL energization.

This work proposes a novel model predictive self-healing control (MPSC) for DAB converter in NSPS with PPLs. The proposed controller takes advantage of the full model of the DAB converter as oppose to using the average model to regulate the DC-Bus voltage and frequency of the NSPS. The proposed control scheme predicts the AC-link inductor current for one-step ahead in horizon of time. There are periodic pulsations in high frequency AC-link inductor's voltage which extremely decrease current prediction accuracy; therefore, two validation modules are developed in this control scheme for correcting the AC-link inductor current. The inductor voltage is monitored by the first validation module and the power transfer is checked to be in the feasible range by the second validation module. The proposed control framework is developed based on root-finding algorithm. The proposed MPSC for DAB converter does not require significant tuning effort compared to conventional PI-based control. The self-healing feature of the MPSC enhances the dynamic performance of controller particularly for extreme PPLs. The fast-dynamic feature of the proposed MPSC ensures the NSPS

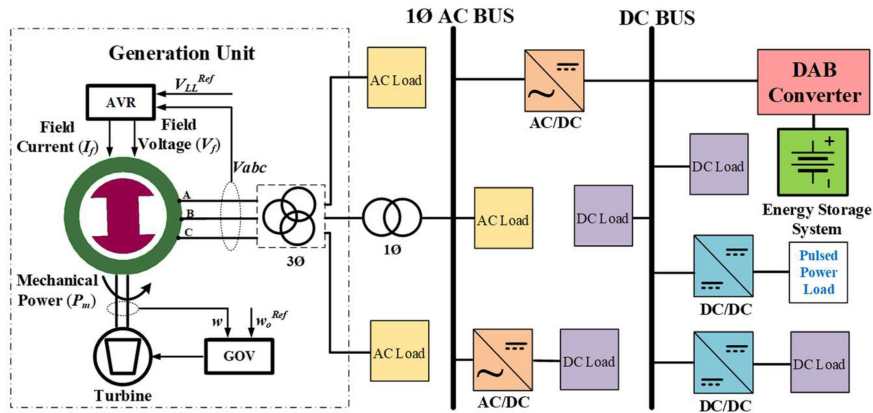


Fig. 1. The considered navy ship power system.

voltage and frequency stability and maximizes its resiliency in response to extreme PPLs.

The remainder of this paper is organized as follows: Section II provides an overview of considered NSPS. In this section, root-cause of voltage and frequency deviations in NSPS, control process by automatic voltage regulator (AVR) and load frequency control (LFC) in generation unit are discussed. Also, an overview of the proposed MPSC for ESS based DAB is provided. Self-healing mechanism, optimal switching selection mechanism of the proposed controller and stability analysis are detailed in Section III. Section IV provides the case studies and results discussion. Finally, this paper is concluded in Section V.

## II. NAVY SHIP POWER SYSTEM: AN OVERVIEW

In conventional ship power systems, the system is based on radial architecture and the loads are supplied by separate generators. As an example of a well-known ship which has this power system architecture is SS Canberra. The propulsion systems are supplied by generators with around 32MW capacity while for services loads, the scale of generator can reach to around 1MW [25]–[27]. Also, some ships use integrated power system (IPS) architecture for their propulsion and services loads; as an example, Queen Elizabeth II has IPS architecture in its power system. The distribution part is operated at 10kV. However, for supplying some services loads, this voltage level is decreased by a step down transformer. Some cruise ships, ferries and vessels follow the IPS architecture with different voltage level in distribution part for increasing the efficiency [25]–[32]. AC zonal electric distribution is another architecture that has been proposed for improving the reliability and efficiency of the ship power system and is known as modern power system for ships [33]–[35]. Also, a DC zonal electric distribution has been considered by Electric Ship Research and Development Consortium (ESRDC) [29], [35]. These two recent types of power system separate the whole system to different zone with independent power supplies. In this work, we have followed this approach to form an AC and DC-Buses representing a hybrid zone of a common navy ship power system. Fig. 1, shows the

TABLE II  
SYNCHRONOUS GENERATOR SPECIFICATIONS

Parameter	Value
Output Voltages	460V
Nominal Power	10.2 kVA
Frequency	60 Hz
Inertia coefficient	0.0923 kg.m <sup>2</sup>
Inertia constant	13117.8 kg.m <sup>2</sup> /sec
Pole pairs	2
Friction Factor	0.0125 N.m.s
Nominal Rotor Speed	1800 RPM

considered hybrid AC/DC NSPS in this paper. The major elements include: synchronous generator unit, ESS interfaced DAB converter, AC loads, DC loads, PPLs, single and three-phase transformers, etc. A synchronous generator supplies the system loads in steady state. Thus, due to slow dynamic response of the main generation unit, any significant change in the system loads such as PPLs energizing, causes a frequency and voltage deviation and consequently lead to instability in the system. The synchronous generator is controlled by two controllers: automatic voltage regulator (AVR) and load frequency control (LFC). A three-phase transformer steps up voltage for supporting medium-voltage loads in NSPS; these loads are energized independently in the system as shown in Fig. 1. A single-phase transformer energizes the AC-Bus to supply single-phase loads and DC-Bus through a DC/AC converter forming a hybrid NSPS. The ESS interfaced DAB converter is connected to the DC-Bus of the NSPS supplying the PPLs.

### A. Root-Cause of Voltage and Frequency Deviation in NSPS

The considered synchronous generator specifications are provided in Table. II. The three-phase synchronous generator has been modelled in the  $dq$  rotor reference frame and stator windings are connected in wye to an internal neutral point [36]. The two control loops of the synchronous generators regulate the output terminal voltage and the frequency. Based on the synchronous generator fundamentals, if for any reasons, the output-power changes suddenly, the whole system frequency will be affected. The root-cause of this issue can be observed by

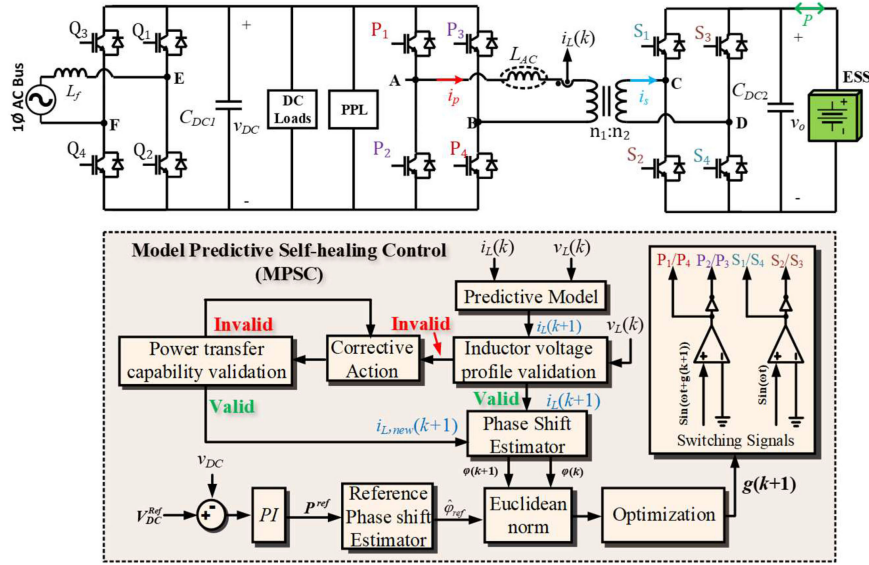


Fig. 2. Structure of the proposed control scheme for dual active bridge converter in navy ship power system.

the swing equation. The rotor motion equation is given by,

$$\theta_m = \omega_s t + \delta_m, \quad (1)$$

where  $\theta_m$  is defined as the angular position of the rotor with respect to a stationary axis,  $\omega_s$  is the synchronous speed and  $\delta_m$  is the angular position with respect to the synchronously rotating reference frame. Thus, the swing equation is given by,

$$P_m - P_e = \omega_m J \frac{d}{dt} \left( \frac{d}{dt} (\omega_s t + \delta_m) \right) \quad (2)$$

where  $P_m$ ,  $P_e$  and  $\omega_m$  are the mechanical power, electrical power and angular velocity of the rotor, respectively. It should be noted that  $\omega_m J$  is defined as the inertia constant of machine at synchronous speed of  $\omega_s$ . The angular momentum of the rotor at synchronous speed is calculated as  $J\omega_s^2$ . Where  $J$  is the inertia coefficient and  $\omega_s$  is the synchronous speed. The inertia constant in this work is 13117.88 kg.m<sup>2</sup>/sec which indicates that the synchronous machines has considerable inertia. Based on (2), the system frequency is vulnerable to sudden changes in power demand due PPLs. The rate of frequency change highly depends on inertia constant of the machine. In this paper, a three-phase PLL is used to obtain the instantaneous frequency; and this value is compared with a desired value and regulated via a PI controller. Furthermore, the generator output voltage is sensitive to load disturbances. By triggering the PPLs, the frequency of the system decreases. In fact, the frequency of the system is related to rotor speed. When the rotor speed decreases, the internal voltage of synchronous generator changes. The induced internal voltage of the generator in a given stator is defined as  $k\phi 2\pi f$ , where  $k$  is a constant related to the structure of the machine,  $\phi$  is the flux, and  $f$  is the frequency. For increasing the internal voltage, the AVR should increase the flux by increasing the field current. However, after a certain value of the field current, the relation of the flux and the field current will not be linear. Therefore, if the load changes suddenly and the frequency drops considerably, the

output voltage of synchronous machine will be affected by this event. Thus, commonly the generator field voltage is controlled via AVR.

### B. Proposed Control Scheme Principle for ESS Based DAB

This section provides a brief overview of the proposed MPSC, the detail control formulation is provided in Section III. The block diagram of the proposed MPSC scheme for DAB converter is depicted in Fig. 2. A DAB converter consists of two H-bridges connected through a high-frequency transformer. The main control goal for DAB converter is to impose a phase shift between the high frequency transformer terminal voltages to permit bidirectional power flow.

The MPSC process is initiated by the AC-link inductor current prediction and it ends by an accurate estimation of desired phase shift to obtain the optimum switching signal. The initial estimation of the phase shift is carried out by a PI controller when required power by ESS is calculated for regulating DC-Bus voltage. The distinctive features of the proposed controller are the two validation modules to heal prediction errors and maximize the accuracy of the phase shift estimation. The first validation module, evaluates the inductor current prediction by monitoring the AC-link inductor voltage for potential prediction errors. If the first validation module detects that the current prediction is not valid, then a corrective action and consequently second validation module are triggered. The second validation module notion is built on the synergy between the power transfer capability of DAB and the value of the phase shift. The corrective action to heal the predicted current occurs between first and second validation modules, once the healing is processed, the resultant predicted current will be sent to second validation module. This process is repeated in an iterative manner to compensate the current prediction and consequently estimate an accurate phase shift.

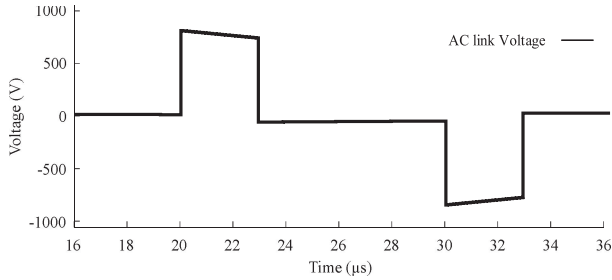


Fig. 3. Typical voltage waveform of dual active bridge converter's AC-link inductor.

The validated predicted AC-link inductor current is used to estimate the phase shift for one step ahead in horizon of time  $\varphi(k+1)$ . The phase shift optimum value is obtained by comparing  $\varphi(k)$  and  $\varphi(k+1)$  with respect to  $\hat{\varphi}_{ref}$  value which is determined by minimization of the Euclidean norm. This optimal phase shift is used to realize the switching signals. The detailed theoretical analysis and mathematical formulation of this self-healing process for the proposed control scheme is provided in the next section.

### III. MODEL PREDICTIVE SELF-HEALING CONTROL

#### A. Self-Healing Mechanism

As mentioned in the previous section, the self-healing mechanism consists of two validation modules. In the first module, inductor voltage is monitored for detecting the potential error in the predicted AC-link inductor current. Fig. 3 depicts the AC-link voltage in one period with an arbitrary phase shift. The output of this module is defined as binary valid and not-valid sections based on the AC-link inductor voltage profile. Considering the relation between AC-link inductor voltage and current and using Euler approximation method, the current of the AC-link inductor for one-step ahead is given by,

$$i_L(k+1) = \frac{v_L(k)}{f_s L_{AC}} + i_L(k), \quad (3)$$

where  $f_s$  is sampling frequency,  $v_L(k)$  and  $i_L(k)$  are the AC-link inductor voltage and current respectively. In order to detect valid and not-valid sections, the AC-link inductor  $L_{AC}$  minimum and maximum voltages are given by,

$$\begin{aligned} v_{L_{\max}} &= v_{AB} + \frac{n_1}{n_2} v_{CD} \\ v_{L_{\min}} &= -v_{AB} - \frac{n_1}{n_2} v_{CD}. \end{aligned} \quad (4)$$

If none of the voltages in (4) are detected, it means there is no prediction error and this validation block sends a binary digit "1"; hence, the controller goes ahead to select the optimum switching. However, if one of the voltages in (4) is detected, it means that there is an error in prediction process and the output of this block will be a binary digit "0" and the second validation module triggers the corrective action mechanism for mitigating the prediction error. The corrective action is based on

an incremental adjustment and is given by,

$$i_{L,new}(k+1) = \frac{v_L(k)}{L_{AC} f_s} + \beta \times i_{L,old}(k+1) + i_L(k) \quad (5)$$

where  $\beta$  is decreased in each iteration incrementally. This process is repeated until the power transfer capability module verifies the predicted current.

The DAB converter's power transfer ability is the basis of the second validation module. A brief overview of power transfer fundamental of DAB is provided in order to clarify the necessity of this validation module. The power transfer fundamental of DAB is similar to power transfer in power system given by,

$$p_r = \frac{v_s v_r}{x} \sin(\delta), \quad (6)$$

where  $v_s$  and  $v_r$  are sending and receiving-end voltages, and  $\delta$  is the difference of the angle of Bus voltages. This equation shows that current direction and magnitude are controlled by adjusting the voltage angle ( $\delta$ ). The concept is used to develop power transfer in DAB converter; though, there are some differences between power transfer in power system and DAB converter. The DAB converter operates at high frequency while the power system operates at a relatively low frequency, i.e. line frequency. Another difference is the square shape voltage of the primary and secondary side of the transformer in DAB converter. Furthermore, the AC-link inductor of the DAB converter can be regarded as the line inductance of (6).

Using (6) in per-unit system and applying aforementioned differences on DAB converter power transferring principle, the DAB converter's AC-link inductor current is as (7),

$$i_L = \frac{v_{CD}}{x} \varphi \left(1 - \frac{\varphi}{\pi}\right) \quad (7)$$

Thus, the power transfer in DAB converter is given by,

$$p_o = \begin{cases} \left(\frac{n_1 v_{AB} v_{CD}}{n_2 x}\right) \left(\varphi - \frac{\varphi^2}{\pi}\right) & \forall \varphi \in [0, \frac{\pi}{2}] \\ \left(\frac{n_1 v_{AB} v_{CD}}{n_2 x}\right) \left(\varphi + \frac{\varphi^2}{\pi}\right) & \forall \varphi \in [-\frac{\pi}{2}, 0] \end{cases} \quad (8)$$

where ( $v_{AB}$ ) and ( $v_{CD}$ ) are DAB terminal voltages and  $\varphi$  is the phase shift between these voltages. One unique aspect of the proposed control scheme is the validation module which is independent to the DAB converter voltage magnitude and the AC-link inductors value – resulting in a dynamic power transfer capability for the MPSC realization. This is tackled by defining a new variable  $\xi$  which normalizes the power transfer equation in (8) by

$$\xi = \frac{n_2 p_o x}{n_1 v_{AB} v_{CD}}, \quad (9)$$

thus, the normalized power transfer is given by,

$$\xi = \begin{cases} \left(\varphi - \frac{\varphi^2}{\pi}\right) & \forall \varphi \in [0, \frac{\pi}{2}] \\ \left(\varphi + \frac{\varphi^2}{\pi}\right) & \forall \varphi \in [-\frac{\pi}{2}, 0] \end{cases} \quad (10)$$

Equation (10) shows that there are two regions of operation for power transferring in DAB converter. When  $0 \leq \varphi \leq \pi/2$ , the power is transferred from DC-Bus to ESS; otherwise, the power direction is reversed and flows from ESS to DC-Bus. Equation (10) is the mathematical explanation of power transfer capability

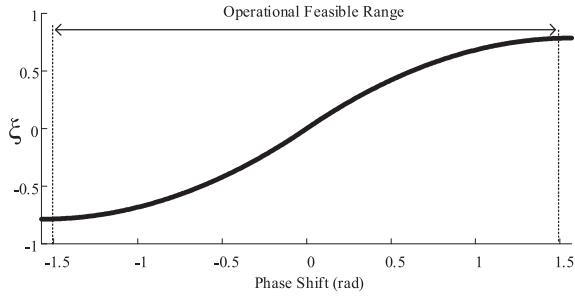


Fig. 4. Dual active bridge converter power transfer capability.

module which is used in self-healing loop and is depicted in Fig. 4.

The output of corrective action process is validated via the determined feasible operation range of DAB converter – power transfer capability. The phase shift between the high frequency transformer terminal voltages of DAB converter is determined by,

$$\varphi(k) = \frac{\pi}{2} \left( 1 - \sqrt{y(k)} \right) \quad (11)$$

where,

$$y(k) = \left( 1 - \frac{8p(k)n_2L_{AC}f_{sw}}{n_1v_{AB}v_{CD}} \right) \quad (12)$$

where  $n_1$  and  $n_2$  are the transformer turns ratio. Hence, the criterion for power transfer capability module is formulated using (8), (11), and (12). The criteria function is given by,

$$f_t(k) = \left( \frac{8p(k)n_2L_{AC}f_{sw}}{n_1v_{AB}v_{CD}} \right) \quad (13)$$

The satisfactory range of  $f_t(k)$  can be determined by solving (11) for its feasible range of  $-\pi/2 \leq \varphi \leq \pi/2$ . This results in the valid range for  $f_t(k)$ ,

$$-3 \leq f_t(k) \leq 1. \quad (14)$$

The power transfer validation module uses (14) as a criterion to validate the corrective action process output for charging process. The derivation of these equations is provided in Appendix section.

### B. Optimal Switching Selection Mechanism

The formulation of the MPSC cost function and optimization procedure is provided in this section. The absolute value of instantaneous AC-link inductor current can be accurately estimated by its RMS value which is given by,

$$IRMS = 2\sqrt{i_0i_m(2D-1) + \frac{(i_0+i_m)^2}{3}(1-D) + \frac{(i_m-i_0)^2}{3}D} \quad (15)$$

where  $i_0$ ,  $i_m$  are the initial and maximum values of the inductor current, respectively. By considering  $D=0.5$  for DAB converter,

equation (15) is simplified as,

$$IRMS = \sqrt{\frac{4}{6} [(i_0^2 + 2i_0i_m + i_m^2) + (i_m^2 - 2i_0i_m + i_0^2)]} \quad (16)$$

Equation (16) can be further simplified given the fact that  $i_0$  is negligible compared to  $i_m$ ,

$$IRMS \cong 1.15 |i_m| \quad (17)$$

By observing the instantaneous AC-link inductor current, it can be seen that the current is almost constant with negligible slope, where the change in current  $\Delta I_{LAC}$  is given by,

$$|\Delta I_{LAC}| = \left| \frac{1-D}{2f_sL_{AC}} \left( v_{AB} - \left( \frac{n_1}{n_2} \right) v_{CD} \right) \right| \quad (18)$$

Thus, the RMS value of AC-link inductor current can be accurately estimated by instantaneous current. In other words, during one switching cycle, the majority of the time,  $|i_m|$  is very close to the absolute value of the instantaneous AC-link inductor current. The phase shift can be estimated based on its relation with RMS value of the AC-link inductor current,

$$|\varphi|^3 + \frac{\pi^3}{4} |\varphi|^2 + \left( \frac{6\pi^3 I_L^2 RMS f_s^2 L^2 AC}{v_{AB}v_{CD}} - \frac{\pi^3}{8} \left( \frac{v_{CD} + v_{AB}}{v_{AB}} \right) \right) = 0 \quad (19)$$

Furthermore, as it is shown in (15)–(18),  $IRMS$  can be substituted by AC-link inductor current instantaneous value in (19). The first potential phase shift  $\varphi(k)$  can be determined by solving (19) using the instantaneous AC-link inductor current. The second potential phase shift  $\varphi(k+1)$  can be determined by solving (19) using the predicted AC-link inductor current given by (3) or (5). The validation modules in the previous section verify the feasibility of the resultant phase shift  $\varphi(k+1)$ . The estimated reference phase shift  $\hat{\varphi}_{ref}$  is determined by regulating the DC-Bus voltage via a PI controller as shown in Fig. 2.

The instantaneous phase shift  $\varphi(k)$ , the predicted phase shift  $\varphi(k+1)$ , and the estimated reference phase shift  $\hat{\varphi}_{ref}$  are used in the Euclidean norm calculation framework for optimization process and determination of the switching signals. This process is depicted in Fig. 5. The optimal switching states that minimize the feasible phase shift  $\varphi(k)$  and  $\varphi(k+1)$  Euclidean norms with the estimated phase shift reference  $\hat{\varphi}_{ref}$  are determined by the proposed cost function. The phase shift vectors based on defined three unity vectors in each sampling time ( $k$ ) are given by,

$$\hat{i} = \frac{\varphi(k)}{|\varphi(k)|}, \hat{j} = \frac{\varphi(k+1)}{|\varphi(k+1)|}, \hat{k} = \frac{\hat{\varphi}_{ref}}{|\hat{\varphi}_{ref}|} \quad (20)$$

$$\vec{\varphi}_k = \varphi(k) \vec{i} + \varphi(k+1) \vec{j}, \vec{\varphi}_{ref} = \hat{\varphi}_{ref} \vec{k}$$

$$\theta(k) = \tan^{-1} \left( \frac{\varphi(k+1)}{\varphi(k)} \right) \quad (21)$$

$\vec{m}_k$  is representing a new vector which is used in the final cost function (g) and it is given by,

$$|\vec{m}_k| = \min \{ |\vec{\varphi}_k| |\sin(\theta(k))|, |\vec{\varphi}_k| \cos(\theta(k)) \} \quad (22)$$

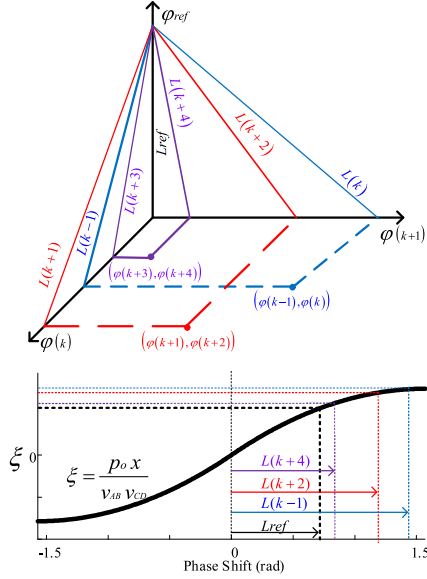


Fig. 5. Graphical representation of the proposed MPSC cost function (g) optimization via Euclidean norm approach.

The direction of  $\vec{m}_k$  will be aligned with  $\hat{j}$  if the first component of (22) has the minimum value; otherwise,  $\vec{m}_k$  direction is aligned with  $\hat{i}$ . Thus, the proposed MPSC cost function (g) for optimization can be formulated as,

$$|g(k+1)| = \sqrt{|\vec{m}_k|^2 + |\vec{\varphi}_{ref}|^2} \quad (23)$$

where (23) obtains the next sampling time ( $k+1$ ) optimum phase shift value. The resultant optimal phase shift by (23) is used to generate the switching signals. The switching signals are generated by the two functions given in (24),

$$\begin{aligned} Y1 &= \sin(2\pi f_{sw} k) \\ Y2 &= \sin(2\pi f_{sw} k + |g(k+1)|) \end{aligned} \quad (24)$$

In more details, the gate signals with the appropriated optimal phase shift are generated by comparing the two function  $Y_1$  and  $Y_2$  with zero. A unique feature of the proposed MPSC is the autonomous determination of the optimal phase shift and accurate estimation of the initial phase shift to be tracked using a root-finding mechanism, this feature enhances the dynamic response of the controller and mitigates the steady state tracking error.

### C. Stability Analysis

Stability of the system is investigated by means of the Lyapunov stability analysis. The next-state converter output phase shift  $\varphi(k+1)$  for optimal tracking is represented by,

$$\varphi(k+1) = \varphi_{opt}(k+1) + e(k+1) \quad (25)$$

where,  $\varphi(k+1)$  is the phase shift which is applied on the transformer terminal voltages and  $\varphi_{opt}(k+1)$  is the phase shift that will produce zero error in DC-Bus voltage in the following time step.  $e(k+1)$  is defined as the phase shift quantization

error. In this case, the magnitude of  $e(k+1)$  is less than or equal to  $l$ , where  $l \in \mathbb{R}^+$ . It is guaranteed that  $l$  is certain to exist and hysteresis bounds with length  $\varphi(k+1)$  is bounded.  $\varphi(k+1)$  remains bounded and this is due to the self-healing mechanism that has been proposed in this work.

$$\|e(k+1)\| \leq l, \quad l \in \mathbb{R}^+. \quad (26)$$

The error in DC-Bus voltage is given by,

$$\begin{aligned} V_{DC\_error} &= V_{DC}(k+1) - V_{DC\_ref}(k+1) \\ V_{DC\_error}(k+1) &= x_L \left[ \frac{v_L(k)}{f_s L_{AC}} + i_L(k) \right] + \frac{n_1}{n_2} v_{cd} \\ &\quad - V_{DC\_ref}(k+1) \end{aligned} \quad (27)$$

The objective of the control is to reduce tracking error asymptotically to zero or to a small error tolerance. The Lyapunov function  $L(k)$  is defined as:

$$L(V_{DC\_error}) = \frac{1}{2} [V_{DC\_error}]^2 \quad (28)$$

Based on Lyapunov theorem for system stability, the time derivative of the Lyapunov function  $\Delta L(V_{DC\_error})$  should be negative for the convergence of  $V_{DC\_error}$  to zero. The time derivative of the Lyapunov function is defined as:

$$\begin{aligned} \Delta L(V_{DC\_error}) &= L(V_{DC\_error}(k+1)) \\ &\quad - L(V_{DC\_error}(k)) \end{aligned} \quad (29)$$

For finding the relation between the next step of AC-link inductor current and the phase shift, AC-link inductor voltage is calculated in term of phase shift based on the DAB converter fundamental and is given by,

$$v_L(k) = \frac{n_1 v_{CD}}{2n_2 \pi} \left( \varphi(k) - \frac{\varphi^2(k)}{\pi} \right) - \frac{L_{AC} 2\pi f_s i_L(k)}{2\pi} \quad (30)$$

Therefore, the next step of AC-link inductor current is calculated by,

$$\frac{v_L(k)}{f_s L_{AC}} + i_L(k) = \frac{n_1 v_{CD}}{n_2 L_{AC} 2\pi f_s} \left( \varphi(k) - \frac{\varphi^2(k)}{\pi} \right) \quad (31)$$

Using (27-31), the time derivative of the Lyapunov function is given by:

$$\begin{aligned} \Delta L(V_{DC\_error}) &= \frac{1}{2} \left[ x_L \left[ \frac{v_L(k)}{f_s L_{AC}} + i_L(k) \right] + \frac{n_1}{n_2} v_{CD}(k+1) - V_{DC\_ref}(k+1) \right]^2 \\ &\quad - \frac{1}{2} [V_{DC\_error}(k)]^2 \end{aligned} \quad (32)$$

considering  $\frac{n_1}{n_2} v_{CD} = \alpha$ , equation (32) is simplified by,

$$\begin{aligned} \Delta L(V_{DC\_error}) &= \frac{1}{2} \left[ \alpha \varphi(k+1) - \frac{\alpha \varphi^2(k+1)}{\pi} - \frac{n_1}{n_2} v_{cd} \right]^2 \\ &\quad - \frac{1}{2} [V_{DC\_error}(k)]^2 \end{aligned} \quad (33)$$

For converging  $V_{DC\_error}$  to zero, it is necessary to find a proper phase shift which satisfy  $\Delta L(V_{DC\_error}) \leq 0$ . Rearranging this inequality results in,

$$\alpha \varphi(k+1) - \frac{\alpha \varphi^2(k+1)}{\pi} - \frac{n_1}{n_2} v_{CD} - V_{DC\_ref}(k+1) \leq V_{DC\_error}(k) \quad (34)$$

Using (27), this equation is simplified by,

$$\varphi^2(k+1) - \pi \varphi(k+1) + \frac{\pi(\alpha + V_{DC}(k+1))}{\alpha} \geq 0 \quad (35)$$

By solving this inequality and considering the DAB phase shift limitation and (25), the phase shift which ensures a negative time derivative of  $\Delta L(V_{DC\_error})$  is defined as  $\varphi(k+1)$  and is given by,

$$\begin{aligned} \varphi_{opt}(k+1) + l &= \frac{\pi \pm \sqrt{\pi^2 - \frac{4\pi}{\alpha}(\alpha + V_{DC}(k+1))}}{2} \\ \varphi_{opt}(k+1) &\geq \frac{\pi}{2} - \sqrt{\frac{\pi^2}{4} - \frac{\pi}{\alpha}(\alpha + V_{DC}(k+1))} - l \\ \varphi(k+1) &= \frac{\pi}{2} - \sqrt{\frac{\pi^2}{4} - \frac{\pi}{\alpha}(\alpha + V_{DC}(k+1))} \quad (36) \end{aligned}$$

The system should meet the following Lyapunov criteria:

$$\begin{aligned} L(V_{DC\_error}(k)) &\geq c_1 |V_{DC\_error}(k)|^\vartheta \quad \forall V_{DC\_error}(k) \in \Upsilon \\ L(V_{DC\_error}(k)) &\geq c_2 |V_{DC\_error}(k)|^\vartheta \quad \forall V_{DC\_error}(k) \in \Gamma \\ L(V_{DC\_error}(k+1)) - L(V_{DC\_error}(k)) &\leq -c_3 |V_{DC\_error}(k)|^\vartheta + c_4 c_1, \quad c_2, c_3, c_4 \in R^+, \\ \vartheta &\geq 1, \quad \Upsilon \in R, \quad \Gamma \subset \Upsilon \quad (37) \end{aligned}$$

Substituting calculated  $\varphi(k+1)$  into (33) and assuming  $\varphi(k+1) = \varphi$ ,

$$\begin{aligned} \Delta L(V_{DC\_error}) &= \frac{1}{2} \left[ \frac{\alpha(\varphi_{opt}(k+1) + l) - \frac{\alpha(\varphi_{opt}(k+1) + l)^2}{\pi}}{-\frac{n_1}{n_2} v_{CD} - V_{DC\_ref}(k+1)} \right]^2 \\ &\quad - \frac{1}{2} [V_{DC\_error}(k)]^2 \\ \Delta L(V_{DC\_error}) &= \frac{1}{2} \left[ \frac{\alpha\varphi - \frac{\alpha}{\pi}\varphi^2 - \alpha - V_{DC\_ref}(k+1)}{+\alpha l - \frac{\alpha}{\pi}(2\varphi l) - \frac{\alpha}{\pi}l^2} \right]^2 \\ &\quad - \frac{1}{2} [V_{DC\_error}(k)]^2 \quad (38) \end{aligned}$$

Based on (36), (38), the bounded form of  $\Delta L(V_{DC\_error})$  is given by,

$$\Delta L(k) \leq \frac{1}{2} \left[ \alpha - \frac{\alpha}{\pi} l - \frac{2\varphi\alpha}{\pi} \right]^2 l^2 - \frac{1}{2} [V_{DC\_error}(k)]^2 \quad (39)$$

Furthermore, the DC-Bus voltage converges to a condensed equation which is given by,

$$\Omega = \left\{ \|V_{DC\_error}(k)\|^2 \leq \left( \alpha - \frac{\alpha}{\pi} l - \frac{2\varphi\alpha}{\pi} \right) l \right\} \quad (40)$$



Fig. 6. OPAL-RT platform HIL setup of NSPS.

TABLE III  
DAB CONVERTER SPECIFICATIONS

Parameter	Value
Input Voltage	400V
Output Voltage	200V
DC Capacitors	1.2mF
Switching Frequency	50 kHz
High Frequency Transformer Turn Ratio	2:1
Secondary Side Leakage Inductor	10 $\mu$ H
AC Link Inductor	5 $\mu$ H

Finally, from (37),

$$c_1 = c_2 = 1; \quad c_3 = 0.5, \quad c_4 = 0.5 \left( \frac{\pi}{\alpha l (\pi - l - 2\varphi)} \right)^2 l^2 \quad (41)$$

Thus, controlled parameter is within a bounded region, and therefore satisfy Lyapunov's stability criterion.

#### IV. CASE STUDIES AND DISCUSSION

Several case studies are carried out in OPAL-RT HIL environment for the NSPS of Fig. 1; the HIL setup is shown in Fig. 6. System specifications for DAB converter has been provided in Table III. The conducted case studies validate the controller performance to the PPLs energization in the NSPS. The overall goal is to maximize the NSPS resiliency by regulating voltage and frequency of the system via the MPSC of DAB converter interfaced ESS. A comparison with conventional PI controller is also provided demonstrating the superiority of the proposed MPSC scheme.

Fig. 7 depicts the DAB converter high frequency transformer's voltage and current waveforms in steady state. Precisely, the high frequency transformer terminal voltages are 50 kHz square wave. Furthermore, a phase shift is observable between the high frequency transformer terminal voltages (see Fig. 7). This phase shift enables the bidirectional power flow capability of the DAB converter. Moreover, Fig. 8 shows the DAB converter high frequency transformer currents in one switching period. PPL has a periodic pattern of a square wave with amplitude of 6 kW, 1 kHz frequency and duty cycle of 40%. It is worthy to mention that when the PPL is triggered, the amplitude of the instantaneous demand is 6 kW (i.e. 0.59 pu) and the average PPL is 2.4 kW (i.e. 0.23 pu). Note that, the PPL is triggered at instant 12s and



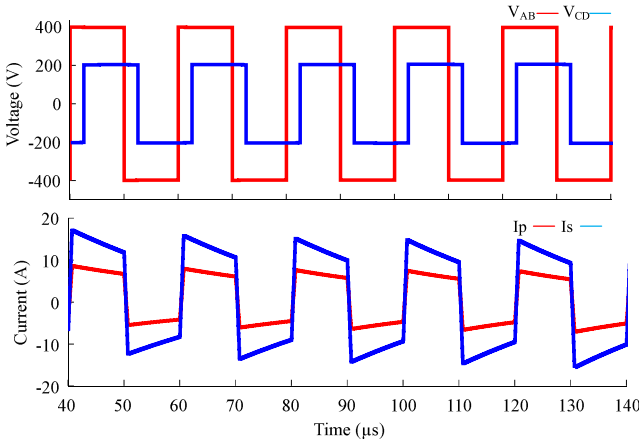


Fig. 7. AC-link transformer's high frequency current and voltage waveforms using MPSC.

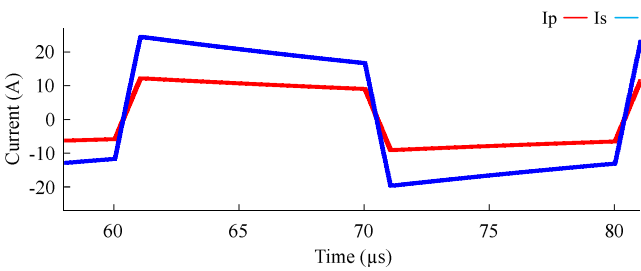


Fig. 8. One cycle ac-link transformer's primary and secondary side current using MPSC.

adds 6 kW to the base load (3 kW) of the system. The base for pu calculations is the nominal apparent power of the synchronous generator. Considering just a single phase of the entire system, the base load has the value of 0.88 pu and the average PPL load which is imposed on the system is about 0.7 pu; thus, when PPLs are triggered, the system faces with serious frequency and voltage challenges; this scenario accurately replicates the model of a critical condition for a system in real-time which is handled by the proposed MPSC scheme. The considered PPL profile is illustrated in Fig. 9a and 9b.

Fig. 10 shows the NSPS DC-Bus voltage when a conventional PI controller is used to control the DAB converters in response to the PPL energization. As it is seen, the DC-Bus voltage is collapsed within 0.2s after energization of the PPL. Fig. 12 shows that the system frequency deviates and then collapses by about 15 Hz when the PPL is triggered. This case study demonstrates that due to slow dynamic response of the DAB based PI-controller, the voltage and frequency of the system collapses and causes loss of loads etc. Although, DAB based PI-controller may have relatively acceptable dynamic response for arbitrary load patterns without pulsating behavior, but its dynamic response is not fast enough to regulate the voltage and frequency of the system in response to PPL energization. This eventually results in voltage and frequency collapse after couple of PPL cycles as it is shown in Figs. 10 and 12.

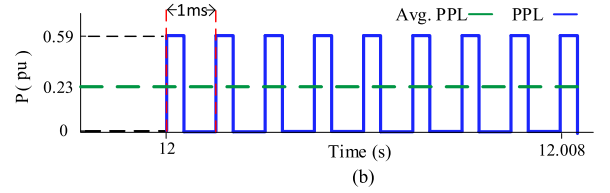
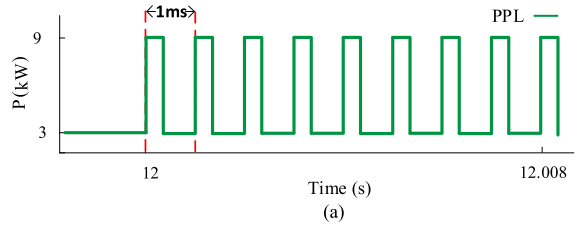


Fig. 9. a) Pulsed power load pattern, triggered at instant 12s. 9(b) Pulsed power load pattern in per unit considering synchronous generator apparent power as base power, triggered at instant 12s.

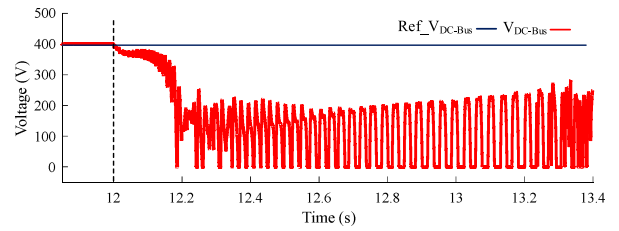


Fig. 10. DC- Bus voltage dynamic using PI controller: the bus voltage collapses after energization of PPL.

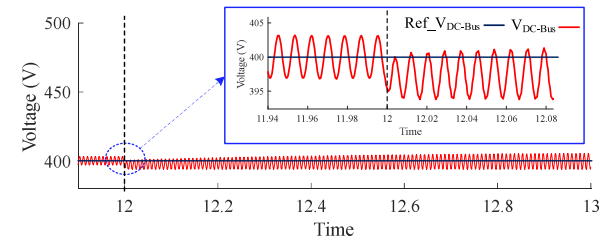


Fig. 11. DC- Bus voltage dynamic using MPSC: the bus voltage restored after energization of PPL.

The proposed controller performance in response to PPL energization is analyzed in Fig. 11 and Fig. 13. The AC-Bus frequency dynamic when using the proposed MPSC is shown in Fig. 13. As it is demonstrated, once the PPL is triggered for energization, there is a deviation in frequency at instant 12s, but the DAB based MPSC restores the system frequency with around 3.5 seconds. Ship classification societies have put restrictions on the frequency deviations from the nominal value in both steady-state and transient conditions [30]. These rules allow a  $\pm 5\%$  deviations from the nominal frequency at steady state. For transient conditions the standard allows  $\pm 10\%$  deviations for a duration of 5 sec and less. Table IV provides standard requirements and metrics for NSPS frequency and voltage regulation. The results are quantified, compared, and listed in Table V. Results show that the proposed MPSC scheme restores the frequency deviation of around 4 Hz, due to the activation of the

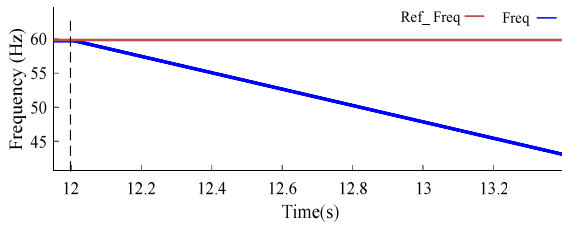


Fig. 12. AC- Bus frequency dynamic using PI controller: the bus frequency collapses after energization of PPL.

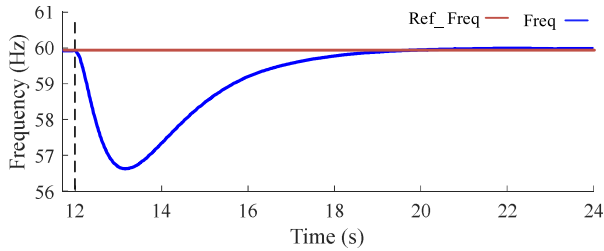


Fig. 13. AC- Bus frequency dynamic using MPSC: the bus frequency restored after energization of PPL.

TABLE IV  
SHIP STANDARDS ALLOWABLE FREQUENCY AND VOLTAGE DEVIATIONS [30]

Variable	Deviation	Duration
Frequency	$\pm 5\%$	Permanent
	$\pm 10\%$	5 sec
Voltage	$-10\% \sim 6\%$	Permanente
	$\pm 20\%$	1.5 sec

TABLE V  
PI AND PROPOSED MPSC FREQUENCY AND VOLTAGE DEVIATION COMPARISON

Variable	PI		MPSC	
	Deviation	Duration	Deviation	Duration
Frequency	Collapses	Permanent	$\pm 4.75\%$	3.5 sec
Voltage	Collapses	Permanent	Negligible	-

PPL, in less than 3.5 seconds which is satisfactory according to the specification defined by the standard for ships. On the other hand, the conventional PI-based controller fails to restore the frequency and voltage to their nominal steady state values. It worth mentioning that, the PPL of 6 kW is a considerable sudden load added to the NSPS Buses.

The impact of PPL energization on the system AC-Bus voltage, derived by synchronous generator, is studied. Fig. 14 demonstrates the generator output voltage dynamic response where the DAB based PI controller is implemented in NSPS. As it is shown, generator and ESS cannot restore the AC-Bus voltage due to PPL pattern in NSPS. In fact, the AVR tries to regulate the generator output voltage; however, due to considerable unbalance between demand and supply and frequency collapse, the generator output voltage cannot follow the desired voltage and the AC-Bus is collapsed; thus, the voltage is not sinusoidal anymore which cause triggering of protection

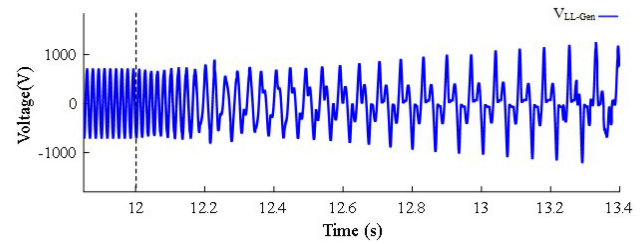


Fig. 14. Generator output voltage dynamic using PI: the generator voltage and consequently AC-Bus voltage collapses after energization of PPL.

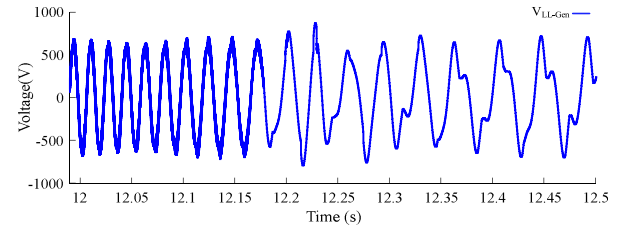


Fig. 15. Zoomed-in Generator output voltage dynamic using PI: the generator voltage and consequently AC-Bus voltage collapses after energization of PPL.

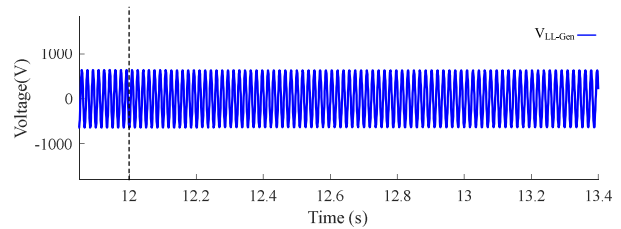


Fig. 16. Generator output voltage dynamic using MPSC: the generator voltage and consequently AC-Bus voltage are regulated and stable after energization of PPL.

relays and eventually results in system shutdown. Fig. 15 is the zoomed-in format of Fig. 14. As it is seen voltage collapse after the PPL is activated. In comparison, the generator output voltage when DAB based MPSC is implemented is shown in Fig. 16. In this case, the generator voltage and consequently the AC-Bus voltage is well-regulated and stable even after energizing PPLs. It is worthy to mention that because DAB based MPSC scheme supports system frequency by compensating the sudden demand in the system, LFC is able to restore the sudden drop in system frequency; therefore, generator output power can increase based on its inherent dynamic response. Also, the AVR adjusts the exciter voltage for supporting any voltage transient during PPLs energization. Fig. 17 is the zoomed-in version of Fig. 16, as it is shown voltage remains stable and sinusoidal after the PPL is activated.

The demand-supply balancing mechanism by the proposed controller is studied next. Fig. 18 shows the dynamic behavior of the total power supplied by generator and ESS as well as their individual power generation when using DAB based MPSC. As it is shown, the overall system resiliency is enhanced by the fast-dynamic response of the DAB based MPSC. The NSPS base load is 3 kW and the PPL is 6 kW with duty cycle of 0.4.

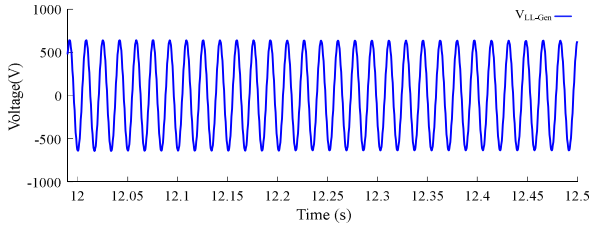


Fig. 17. Zoomed-in Generator output voltage dynamic using MPSC: the generator voltage and consequently AC-Bus voltage are regulated and stable after energization of PPL.

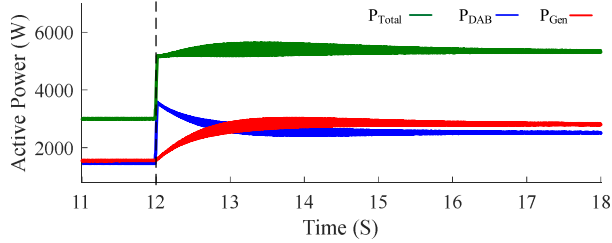


Fig. 18. Active power dynamic of synchronous generator, DAB based MPSC and the total generation.

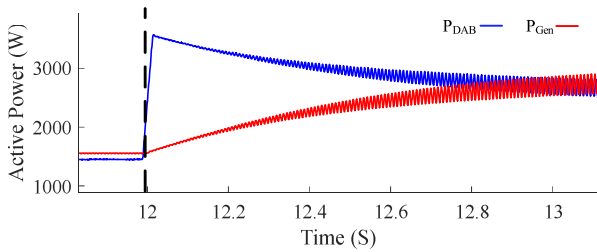


Fig. 19. Active power dynamic of synchronous generator, DAB based MPSC zoomed-in around instant 12s.

Therefore, before PPL energization, the ESS and synchronous generator should supply the 3kW demand. By energizing the PPL, the average PPL increases to around 5.4 kW considering PPL duty cycle in steady state. Moreover, Fig. 19 shows the dynamic responses of the proposed controller and synchronous generator in response to sudden load change. As it is shown, the synchronous generator needs about 2s to regulate its output power to compensate increased demand, while the gap between demand and supply is compensated in less than 0.1s by fast dynamic response of ESS interfaced with DAB based MPSC.

## V. CONCLUSION

This paper addresses the challenges associated with design of MPC framework for DAB in NSPS in response to voltage and frequency deviations due to PPL energization. A model predictive self-healing control scheme is proposed for a DAB converter that is interfacing ESS to the DC-Bus in a hybrid AC/DC NSPS with PPL. The proposed controller is able to keep the NSPS voltage and frequency regulated and stable particularly when a considerable PPL is energized – enhancing the system resiliency to PPL energization. The proposed MPSC tackles

the challenges and drawbacks associated with MPC framework for DAB converters while leveraging its inherent fast dynamic response to address the voltage and frequency deviation in NSPS with PPL. The proposed controller main characteristics are the two validation modules to mitigate the possible error in the predicted AC-link inductor current of DAB converter. This unique aspect of the proposed approach enables robust implementation of predictive control for DAB converter with inherent pulsating AC-link inductor voltage at high frequency. A cost function is developed to determine the possible switching states that minimizes the Euclidean norm of the possible phase shift with respect to the estimated phase shift reference. It is proved that the implemented estimating block in the proposed controller have high accuracy. Several case studies are conducted in HIL environment to evaluate the functionality of the proposed DAB based MPSC in NSPS and validate its ability to enhance the system resiliency by restoration of voltage and frequency when PPL is energized. The provided case studies demonstrate the superiority of the proposed MPSC compared to PI based controller for ESS interfaced DAB converter in NSPS.

## APPENDIX

This appendix firstly provides a detail analysis for necessity of a self-healing mechanism for conventional MPC for DAB converter. The imposed voltage on AC-link inductor is given by,

$$v_L(k) = v_{AB} - \frac{n_1}{n_2}(v_{CD}) \quad (42)$$

Based on the phase shift applied to the transformer terminal voltages, two short time slots in every switching cycle are formed (Fig. 7), when  $v_{AB}$  has positive value and  $v_{CD}$  has negative value, the imposed voltage on AC-link inductor is given by,

$$v_{L_{\max}} = v_{AB} + \frac{n_1}{n_2}v_{CD} \quad (43)$$

when  $v_{AB}$  has negative value and  $v_{CD}$  has positive value; the imposed voltage on the inductor is calculated by,

$$v_{L_{\min}} = -v_{AB} - \frac{n_1}{n_2}v_{CD} \quad (44)$$

While the imposed voltage on the AC-link inductor is zero approximately rest of the time. When a pulsation in current occurs, the predicted phase shift can have invalid value. For clarifying this issue, it is proved that why these pulsations cause the phase shift to be invalid. The phase shift for charging process is given by,

$$\varphi(k) = \frac{\pi}{2} \left( 1 - \sqrt{\left( 1 - \frac{8p(k)n_2L_{AC}f_{sw}}{n_1v_{AB}v_{CD}} \right)} \right) \quad (45)$$

In order to have a valid value for phase shift, the basic constraint for this equation is given by,

$$1 - \frac{8p(k)n_2L_{AC}f_{sw}}{n_1v_{AB}v_{CD}} \geq 0 \quad (46)$$

Considering the primary winding of high frequency transformer as high voltage side, the following equation is valid

always. This is given by,

$$v_{AB} + \frac{n_1}{n_2} v_{CD} \geq v_{AB} + v_{CD} \quad (47)$$

Satisfying the equality constraint, the next step of maximum predicted AC-link inductor current is given by,

$$i_{L_{\max}}(k+1) = \frac{v_{AB} + v_{CD}}{f_s L_{AC}} + i_L(k) \quad (48)$$

Hence, the amount of power that is transferred through DAB converter is calculated by,

$$p(k+1) = \frac{v_{AB}^2 + v_{AB}v_{CD}}{f_s L_{AC}} + v_{AB}i_L(k) \quad (49)$$

Checking this equation by the constraint in (46) results in,

$$\frac{v_{AB}^2 + v_{AB}v_{CD}}{f_s L_{AC}} + v_{AB}i_L(k) \leq \frac{n_1 v_{AB} v_{CD}}{8 n_2 L_{AC} f_{sw}} \quad (50)$$

After simplifying the inequality and considering  $k^\dagger = f_s/8 f_{sw}$ , equation (50) is rewritten by,

$$v_{AB} + v_{CD}(1 - k^\dagger) + f_s L_{AC} i_L(k) \leq 0 \quad (51)$$

According to fig. 7, there are instants that results in positive values for all terms in (51) and violates the inequality. Hence, it is proved that the phase shift will not have a valid value and the conventional MPC algorithm fails to proceed. Considering the inequality in (47), the condition for satisfying (46) become worse and this is due to the increase in the inductor current.

Furthermore, this appendix provides the detailed derivation of the equations (11)-(14). Equation (52) represents the restrictions in the phase shift values for determining the power transfer in DAB converter,

$$p_o = \begin{cases} \left( \frac{n_1 v_{AB} v_{CD}}{n_2 x} \right) \left( \varphi - \frac{\varphi^2}{\pi} \right) & \forall \varphi \in [0, \frac{\pi}{2}] \\ \left( \frac{n_1 v_{AB} v_{CD}}{n_2 x} \right) \left( \varphi + \frac{\varphi^2}{\pi} \right) & \forall \varphi \in [-\frac{\pi}{2}, 0] \end{cases} \quad (52)$$

Now, by determining  $\varphi$  in term of power transfer,

$$\varphi = \frac{\pi \pm \sqrt{\pi^2 - 4\pi \frac{p_o n_2 x}{n_1 v_{AB} v_{CD}}}}{2} \quad (53)$$

valid range of phase shift in charging process is analyzed. It means that whenever  $\xi$  as the normalized power is zero, the phase shift should be zero too; also, when the normalize power is  $\frac{\pi}{4}$ , the phase shift should reach to  $\frac{\pi}{2}$  which is the maximum accepted phase shift. For discharging interval, the same process is repeated. However, in order to find a unique criterion for this problem and decreasing computational process in the core of self-healing module, the feature of an odd function has been used; it is stated that the function  $f(x)$  is odd if,

$$f(x) + f(-x) = 0 \quad (54)$$

this equation is valid if the domain of the function is symmetrical. Also,  $f(0) = 0$ , if and only if  $x = 0$  is in the domain of this function. Checking the power transferring function, it is realized that,

$$\varphi = \begin{cases} \frac{\pi - \sqrt{\pi^2 - 4\pi \frac{p_o n_2 x}{n_1 v_{AB} v_{CD}}}}{2} & \forall \xi \in [0, \frac{\pi}{4}] \\ \frac{-\pi + \sqrt{\pi^2 + 4\pi \frac{p_o n_2 x}{n_1 v_{AB} v_{CD}}}}{2} & \forall \xi \in [-\frac{\pi}{4}, 0] \end{cases} \quad (55)$$

By rearranging this function, it is explained as,

$$\varphi = \begin{cases} \frac{\pi}{2} - \sqrt{\frac{\pi^2}{4} \left( 1 - \frac{8 p_o n_2 L_{AC} \pi f_{sw} n_1 v_{AB} v_{CD}}{\pi} \right)} & \forall \xi \in [0, \frac{\pi}{4}] \\ \frac{-\pi}{2} + \sqrt{\frac{\pi^2}{4} \left( 1 + \frac{8 p_o n_2 L_{AC} \pi f_{sw} n_1 v_{AB} v_{CD}}{\pi} \right)} & \forall \xi \in [-\frac{\pi}{4}, 0] \end{cases} \quad (56)$$

In a simplified form, this equation is given by

$$\varphi = \begin{cases} \frac{\pi}{2} \left( 1 - \sqrt{1 - \frac{8 p_o n_2 L_{AC} f_{sw}}{n_1 v_{AB} v_{CD}}} \right) & \forall \xi \in [0, \frac{\pi}{4}] \\ \frac{-\pi}{2} \left( 1 - \sqrt{1 + \frac{8 p_o n_2 L_{AC} f_{sw}}{n_1 v_{AB} v_{CD}}} \right) & \forall \xi \in [-\frac{\pi}{4}, 0] \end{cases} \quad (57)$$

Considering  $ft(k) = \frac{8 p_o n_2 L_{AC} f_{sw}}{n_1 v_{AB} v_{CD}}$  and the fact that  $-\pi/2 \leq \varphi \leq \pi/2$ , the optimal range for  $ft(k)$  in both charging and discharging process are given by,

$$\begin{aligned} \frac{-\pi}{2} &\leq \frac{\pi}{2} \left( 1 - \sqrt{1 - \frac{8 p_o n_2 L_{AC} f_{sw}}{n_1 v_{AB} v_{CD}}} \right) \leq \frac{\pi}{2} \\ \frac{-\pi}{2} &\leq \frac{-\pi}{2} \left( 1 - \sqrt{1 + \frac{8 p_o n_2 L_{AC} f_{sw}}{n_1 v_{AB} v_{CD}}} \right) \leq \frac{\pi}{2} \end{aligned} \quad (58)$$

By rearranging the first inequality,  $-3 \leq ft(k) \leq 1$ ; and for the second one, rearranging the inequality results in  $-1 \leq ft(k) \leq 3$ ; In the self-healing process, the algorithm checks the constraints based on the power transferring direction, features of the odd function, and the overlapped region of two inequalities.

## REFERENCES

- [1] W. W. Weaver, R. D. Robinett, D. G. Wilson, and R. C. Matthews, "Metastability of pulse power loads using the hamiltonian surface shaping method," *IEEE Trans. Energy Convers.*, vol. 32, no. 2, pp. 820–828, Jun. 2017.
- [2] D. A. M. Al-Falahi, T. Tarasiuk, G. S. Jayasinghe, Z. Jin, H. Enshaei, and M. J. Guerrero, "AC ship microgrids: Control and power management optimization," *Energies*, vol. 11, no. 6, 2018.
- [3] T. Van Vu, D. Gonsoulin, F. Diaz, C. S. Edrington, and T. El-Mezyani, "Predictive control for energy management in ship power systems under high-power ramp rate loads," *IEEE Trans. Energy Convers.*, vol. 32, no. 2, pp. 788–797, Jun. 2017.
- [4] T. Tarasiuk and M. Gorniak, "Load sharing in ship microgrids under nonsinusoidal conditions—Case study," *IEEE Trans. Energy Convers.*, vol. 32, no. 2, pp. 810–819, Jun. 2017.
- [5] G. S. Jayasinghe, L. Meegahapola, N. Fernando, Z. Jin, and M. J. Guerrero, "Review of ship microgrids: System architectures, storage technologies and power quality aspects," *Inventions*, vol. 2, no. 1, 2017.
- [6] A. Boveri, F. Silvestro, M. Molinas, and E. Skjong, "Optimal sizing of energy storage systems for shipboard applications," *IEEE Trans. Energy Convers.*, vol. 34, no. 2, pp. 801–811, Jun. 2019.
- [7] S. G. Jayasinghe, D. M. Vilathgamuwa, and U. K. Madawala, "Direct integration of battery energy storage systems in distributed power generation," *IEEE Trans. on Energy Convers.*, vol. 26, no. 2, pp. 677–685, Jun. 2011.
- [8] Q. Xiao, L. Chen, H. Jia, P. W. Wheeler, and T. Dragičević, "Model predictive control for dual active bridge in naval DC microgrids supplying pulsed power loads featuring fast transition and online transformer current minimization," *IEEE Trans. Ind. Electron.*, vol. 67, no. 6, pp. 5197–5203, Jun. 2020.
- [9] J. Hu, P. Joebges, G. C. Pasupuleti, N. R. Averous, and R. W. De Doncker, "A maximum-output-power-point-tracking-controlled dual-active bridge converter for photovoltaic energy integration into MVDC grids," *IEEE Trans. Energy Convers.*, vol. 34, no. 1, pp. 170–180, Mar. 2019.
- [10] F. Xue, R. Yu, and A. Q. Huang, "A 98.3% efficient GaN isolated bidirectional DC–DC converter for DC Microgrid energy storage system applications," *IEEE Trans. Ind. Electron.*, vol. 64, no. 11, pp. 9094–9103, Nov. 2017.

- [11] T. Zhao, G. Wang, S. Bhattacharya, and A. Q. Huang, "Voltage and power balance control for a cascaded H-bridge converter-based solid-state transformer," *IEEE Trans. Power Electron.*, vol. 28, no. 4, pp. 1523–1532, Apr. 2013.
- [12] W. L. Malan, D. M. Vilathgamuwa, and G. R. Walker, "Modeling and control of a resonant dual active bridge with a tuned CLLC network," *IEEE Trans. Power Electron.*, vol. 31, no. 10, pp. 7297–7310, Oct. 2016.
- [13] Z. Shan and J. Jatskevich, "Digital and analog implementations of nonlinear-feedforward controller for a dual-active-bridge converter," in *Proc. IEEE ECCE*, Sep. 20–24, 2015, pp. 4337–4342.
- [14] X. Li and Y. Li, "An optimized phase-shift modulation for fast transient response in a dual-active-bridge converter," *IEEE Trans. Power Electron.*, vol. 29, no. 6, pp. 2661–2665, Jun. 2014.
- [15] G. G. Oggier, M. Ordóñez, J. M. Galvez, and F. Luchino, "Fast transient boundary control and steady-state operation of the dual active bridge converter using the natural switching surface," *IEEE Trans. Power Electron.*, vol. 29, no. 2, pp. 946–957, Feb. 2014.
- [16] D. Segaran, D. G. Holmes, and B. P. McGrath, "Enhanced load step response for a bidirectional DC–DC converter," *IEEE Trans. Power Electron.*, vol. 28, no. 1, pp. 371–379, Jan. 2013.
- [17] Z. Li, Y. Xia, C. Su, J. Deng, J. Fu, and W. He, "Missile guidance law based on robust model predictive control using neural-network optimization," *IEEE Trans. Neural Netw. Learn. Syst.*, vol. 26, no. 8, pp. 1803–1809, Aug. 2015.
- [18] W. Alhosaini, Y. Wu, and Y. Zhao, "An enhanced model predictive control using virtual space vectors for grid-connected three-level neutral-point clamped inverters," *IEEE Trans. Energy Convers.*, vol. 34, no. 4, pp. 1963–1972, Dec. 2019.
- [19] S. Vazquez, J. Rodriguez, M. Rivera, L. G. Franquelo, and M. Norambuena, "Model predictive control for power converters and drives: advances and trends," *IEEE Trans. Ind. Electron.*, vol. 64, no. 2, pp. 935–947, Feb. 2017.
- [20] S. Vazquez *et al.*, "Model predictive control: A review of its applications in power electronics," *IEEE Ind. Electron. Mag.*, vol. 8, no. 1, pp. 16–31, Mar. 2014.
- [21] Y. Zhang and H. Yang, "Model-predictive flux control of induction motor drives with switching instant optimization," *IEEE Trans. Energy Convers.*, vol. 30, no. 3, pp. 1113–1122, Sep. 2015.
- [22] J. Rodriguez *et al.*, "State of the art of finite control set model predictive control in power electronics," *IEEE Trans. Ind. Informat.*, vol. 9, no. 2, pp. 1003–1016, May 2013.
- [23] S. Dutta, S. Hazra, and S. Bhattacharya, "A digital predictive current-mode controller for a single-phase high-frequency transformer-isolated dual-active bridge DC-to-DC converter," *IEEE Trans. Ind. Electron.*, vol. 63, no. 9, pp. 5943–5952, Sep. 2016.
- [24] L. Chen *et al.*, "Moving discretized control set model-predictive control for dual-active bridge with the triple-phase shift," *IEEE Trans. Power Electron.*, vol. 35, no. 8, pp. 8624–8637, Aug. 2020.
- [25] "Report on the Investigation of the Catastrophic Failure of a Capacitor in the AFT Harmonic Filter Room on Board RMS Queen Mary 2 while Approaching Barcelona on 23 September 2010. Report No 28/2011.
- [26] Rules for Classification Ships, Part 4 Systems and components, Chapter 8 Electrical installations. Det Norske Veritas GL Edition: Høvik, Norway, 2011.
- [27] J. Wolfe and M. J. Roa, "Advanced methods for tabulation of electrical loads during special modes of marine vessel operation," *IEEE Trans. Industry Appl.*, vol. 53, no. 1, pp. 667–674, Jan./Feb. 2017.
- [28] T. J. McCoy, "Trends in ship electric propulsion," in *Proc. IEEE Power Eng. Soc. Summer Meeting*, Jul. 21–25, 2002, pp. 343–346.
- [29] J. S. Chalfant and C. Chrysostomidis, "Analysis of various all-electric-ship electrical distribution system topologies," in *Proc. IEEE Elect. Ship Technologies Symp.*, Apr. 10–13, 2011, pp. 72–77.
- [30] American Bureau of Shipping. International Naval Ships, Guide for Building and Classing, Part 4 Vessel Systems and Machinery, American Bureau of Shipping; 2016 International Association of Classification Societies, Requirements Concerning Electrical and Electronic Installations; IACS Req.: Houston, TX, USA, 2016.
- [31] G. Sulligoi *et al.*, "Naval smart grid: Integrated Power System for all electric naval vessels with control and reliability characteristics," in *Proc. AEIT*, Sep. 18–19, 2014, pp. 1–6.
- [32] E. Skjong, E. Rødskar, M. Molinas, T. A. Johansen, and J. Cunningham, "The marine vessel's electrical power system: from its birth to present day," *Proc. IEEE*, vol. 103, no. 12, pp. 2410–2424, 2015.
- [33] H. Hegner and B. Desai, "Integrated fight through power," in *Proc. IEEE Power Eng. Soc. Summer Meet.*, Jul. 21–25, 2002, pp. 336–339.
- [34] M. W. Rose and R. M. Cuzner, "Fault isolation and reconfiguration in a three-zone system," in *Proc. IEEE ESTS*, Jun. 21–24, 2015, pp. 409–414.
- [35] S. Bose, B. Natarajan, C. Scoglio, S. Das, and N. N. Schulz, "Analysis of robustness for shipboard power system with non-radial power flow," in *Proc. IEEE Elect. Ship Tech. Symp.*, Apr. 10–13, 2011 pp. 181–186.
- [36] J. G. Ciezki and R. W. Ashton, "Selection and stability issues associated with a navy shipboard DC zonal electric distribution system," *IEEE Trans. Power Del.*, vol. 15, no. 2, pp. 665–669, Apr. 2000.



**Mohsen Hosseinzadehtaher** (Student Member, IEEE) received the M.Sc. degree in electrical engineering from the Amirkabir University of Technology, Tehran, Iran, in 2014. From 2018 to 2020, he was a Ph.D. Student in Electrical and Computer Engineering Department at Kansas State University, Manhattan, USA. Since 2020, he is pursuing the Ph.D. degree in Electrical and Computer Engineering Department at University of Illinois at Chicago, USA.

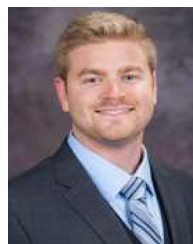
Mr. Hosseinzadehtaher received the best paper award in the 2nd IEEE SGRE conference in 2019. He

is the co-recipient of the "2019 IEEE Foundation Industry Application Society Myron-Zucker Grant".



**Ahmad Khan** (Student Member, IEEE) received the B.Sc. and M.Sc. degrees in electrical engineering from Qatar University, Doha, Qatar in 2014 and 2017, respectively. From 2018 to 2020, he was a Ph.D. Student in Electrical and Computer Engineering Department at Kansas State University, Manhattan, USA. Since 2020, he is pursuing the Ph.D. degree in Electrical and Computer Engineering Department at University of Illinois at Chicago, USA.

Mr. Khan received the Qatar University outstanding thesis award in 2017. He received the best paper award from IEEE IES in the 12th CPE-POWERENG and the 2nd SGRE conferences in 2018 and 2019, respectively. He is co-recipient of the "2019 IEEE Foundation Industry Application Society Myron-Zucker Grant".



**Mitchell Easley** (Student Member, IEEE) received the B.S. degree in electrical engineering from Kansas State University, Manhattan, KS, in 2018, where he is currently pursuing the M.S. degree with the Department of Electrical and Computer Engineering. Since 2017, he has been a Research Associate with the Power Electronics and Autonomous Systems Research Laboratory, Kansas State University. His current research interests include model predictive control, wide bandgap-based power converters, and multilevel converters.



**Mohammad B. Shadmand** (Senior Member, IEEE) received the Ph.D. degree in electrical engineering from Texas A&M University, College Station, USA, in 2015. From 2015 to 2016, he was an Instructor with the Department of Electrical and Computer Engineering, Texas A&M University, College Station, USA. From 2016 to 2017, he was a Research Engineer with the Renewable Energy and Advanced Power Electronics Research Laboratory, College Station, USA. From 2017 to 2020, he was an Assistant Professor with the Department of Electrical and Computer Engineering, Kansas State University, Manhattan, USA. Since 2020, he is an Assistant Professor with the Department of Electrical and Computer Engineering at University of Illinois at Chicago, USA. His current research interests include advanced model predictive control, grid-tied power electronics interfaces with advanced functionalities, grid situational awareness, and control of smart micro-grid systems.

Dr. Shadmand was awarded Michelle Munson Serban Simu Keystone Research Scholar, Kansas State University in 2017. He was awarded the 2019 IEEE Myron Zucker Faculty-Student Research Grant. He has served as Technical Program Co-Chair of the 2019 IEEE Smart Grid & Renewable Energy Conference. He serves as Associate Editor of IEEE TRANSACTIONS ON INDUSTRY APPLICATION and *IET Renewable Power Generation*.



**Poria Fajri** (Member, IEEE) received the B.S. degree in electronics from Urmia University, Urmia, Iran, in 2005, the M.S. degree in electrical engineering from the University of Tehran, Tehran, Iran, in 2008, and the Ph.D. degree in electrical engineering from the Missouri University of Science and Technology, Rolla, MO, USA, in 2014. From 2014 to 2015, he was a Postdoctoral Research Associate at North Carolina State University, Raleigh, NC, USA. From 2015 to 2016 he was a Principal Scientist at Toyota Research Institute of North America, Ann Arbor, MI, USA.

He is currently an Assistant Professor with the Department of Electrical and Biomedical Engineering, University of Nevada, Reno, NV, USA. His research interests include electric-drive vehicles, energy management, renewable energy systems, flexible AC transmission systems, and smart grid.